Frequency spectrum of the geomagnetic field harmonic coefficients from dynamo simulations

C. Bouligand,[1] N. Gillet,[1] D. Jault,[1] N. Schaeffer,[1] A. Fournier[2] and J. Aubert[2]

[1]*Univ. Grenoble Alpes, CNRS, ISTerre, F-38000 Grenoble, France. E-mail: Claire.Bouligand@univ-grenoble-alpes.fr*
[2]*Institut de Physique du Globe de Paris, Sorbonne Paris Cité, Univ. Paris Diderot, CNRS, 1 rue Jussieu, F-75005 Paris, France*

SUMMARY

The construction of geomagnetic, archaeomagnetic or palaeomagnetic field models requires some prior knowledge about the actual field, which can be gathered from the statistical properties of the field over a variety of length-scales and timescales. However, available geomagnetic data on centennial to millennial periods are too sparse to infer directly these statistical properties. We thus use high-resolution numerical simulations of the geodynamo to test a method for estimating the temporal power spectra (or equivalently the autocovariance functions) of the individual Gauss coefficients that describe the geomagnetic field outside the Earth's fluid outer core. Based on the spectral analysis of our simulations, we argue that a prior for the observational geomagnetic field over decennial to millennial periods can be constructed from the statistics of the field during the short satellite era. The method rests on the assumption that time-series of spherical harmonic coefficients can be considered as realizations of stationary and differentiable stochastic processes, namely order 2 autoregressive (AR2) processes. In the framework of these processes, the statistics of Gauss coefficients are well constrained by their variance and one or two timescales. We find that the time spectra in the dynamo simulations of all Gauss coefficients but the axial dipole are well approximated by the spectra of AR2 processes characterized by only one timescale. The process parameters can simply be deduced from instantaneous estimates of the spatial power spectra of the magnetic field and of its first time derivative. Some deviations of the Gauss coefficients statistics from this minimal model are also discussed. Characterizing the axial dipole clearly requires a more sophisticated AR2 process, with a second distinct timescale.

Key words: Time-series analysis; Inverse theory; Probability distributions; Dynamo: theories and simulations; Magnetic field; Rapid time variations.

1 INTRODUCTION

The construction of global field models or of regional master-curves from geomagnetic records has required the use of spatial and temporal regularizations (e.g. Jackson *et al.* 2000; Korte *et al.* 2009; Thébault & Gallet 2010). Searching for models as smooth as possible (e.g. Constable & Parker 1988a) allows to retrieve the features that are reliably constrained by the data, but does not give access to uncertainties on model coefficients. To address this issue, geomagnetic models have been produced using prior information in the form of covariance matrices for the model parameters. These matrices have been built using either some knowledge of the temporal variability of the present geomagnetic field, which we will further discuss here, or spatial cross-covariances deduced from geodynamo simulations (e.g. Fournier *et al.* 2013, 2015). Such prior information is particularly useful when modelling the Earth's magnetic field on historical and archaeological timescales, for which the data distri-

bution is sparse in both space and time, and is characterized by large measurements (and sometimes dating) errors. Finally, prior information in the form of covariance matrices is a prerequisite for data assimilation. For instance, knowledge of the analysis covariance matrix in sequential assimilation is necessary to forecast future trajectories of the geomagnetic field (e.g. Aubert 2015; Gillet *et al.* 2015).

In the probabilistic framework of assimilation algorithms, geomagnetic spherical harmonic coefficients are assumed to result from Gaussian processes. These are stationary stochastic processes fully specified by their means and autocovariance functions (MacKay 1998). As a matter of fact, the autocovariance function of any stationary stochastic process can be deduced from its frequency spectrum. Analyses of geomagnetic records suggest that their power spectrum P behaves as $P(f) \propto f^{-s}$ in some ranges of frequency f, with s the spectral index (e.g. Constable & Johnson 2005; Panovska *et al.* 2013). This defines scale invariance. The index value is related

to the underlying physical processes and to the statistical properties of the time-series.

Studies of the Earth dipole moment (Constable & Johnson 2005) suggest a flat energy density spectrum ($s = 0$) for the longest timescales (1 Myr or more). This spectrum steepens towards higher frequencies, with a spectral index $s \simeq 2$ at millennial to centennial timescales (Panovska *et al.* 2013) and $s \simeq 4$ from centennial to inter-annual timescales (De Santis *et al.* 2003). Considering the unsigned dipole moment for the past 2 Myr, Brendel *et al.* (2007) and Buffett *et al.* (2013) found that its spectrum, over millennial periods, has also a spectral index of 2, and made the analogy with spectra from realizations of autoregressive stochastic processes of order one (AR1). These processes have continuous but non differentiable samples. They are also known as Ornstein-Uhlenbeck processes and are solutions of a Langevin-type equation (Gardiner 1985). Buffett *et al.* (2013) argued that the characteristic timescale of the deterministic part of the stochastic process that they constructed from dipole series is set by the dipole decay time t_d. In this framework, this time is related to the escape time for bistable systems that they also connect to the rate of magnetic reversals. Buffett (2015) also studied the relation of this time to the duration of polarity transitions.

Although the axial dipole field has been the focus of many studies, the non-dipolar field is much less documented. On timescales shorter than a few centuries, order 2 autoregressive (AR2) stochastic processes, whose samples are differentiable, have been introduced to define prior information about the autocovariance function of the Gauss coefficients when building global magnetic field models over the observatory era (Gillet *et al.* 2013) and regional models over archaeological periods (Hellio *et al.* 2014). They are indeed consistent with a spectral index $s = 4$ at decadal periods. Gillet *et al.* (2013) characterized the appropriate AR2 stochastic process from the variance and the secular variation times of the spherical harmonic coefficients. They calculated these two quantities from the geomagnetic spatial power spectrum of the geomagnetic field (Lowes 1974) and of its time-derivative (the secular variation) obtained from a field model of the well documented satellite era. Considering geomagnetic series as sample functions of stochastic processes with power spectrum $P(f) \propto f^{-4}$ gives an explanation to the occurrence of geomagnetic jerks, which are defined as abrupt changes in the geomagnetic field second time derivative (Mandea *et al.* 2010).

Constructing field models from realizations of AR2 processes yields time-series very similar to observatory series (Brown 2015). However, the hypothesis that Gauss coefficients can be described in terms of AR2 stochastic processes is not easily tested using geomagnetic observations because we lack highly accurate, dense coverage data over a long enough time window. In particular, the satellite era is too short in comparison with the decadal to centennial correlation times involved in the evolution of the geomagnetic field. For this reason, it may be helpful to investigate the statistics of individual coefficient series from numerical simulations of the geodynamo. Although calculated for dimensionless numbers far from Earth-like parameters, numerical simulations provide us with time-series of Gauss coefficients that may be used to test assumptions about the statistics of the field coefficients (Kuipers *et al.* 2009; Tanriverdi & Tilgner 2011; Meduri & Wicht 2016). A major issue is the rescaling of the time axis (Lhuillier *et al.* 2011b; Christensen *et al.* 2012). Buffett *et al.* (2014) and Buffett & Matsui (2015) have just achieved a comparison between the frequency spectrum of the dipole term obtained from a numerical simulation and the theoretical spectrum expected for a stochastic process. In both numerical and theoretical

spectra, they distinguished three domains of increasing frequencies for which the spectral index is, as described above for the observed field, $s = 0$, $s = 2$ and $s = 4$. Then, they documented the transitions between the three frequency ranges, and proposed a phenomenological interpretation of the two cut-off times: they suggest that they are related to the dipole decay time t_d and to the lifetime of convective eddies in the fluid core. Attributing the different times to specific underlying mechanisms in the geodynamo models may help to compare simulations and observations and to overcome the limitations of the numerical models.

Instead of focusing our analysis on the dipole field, we apply here stochastic modelling to spherical harmonics of higher degree. We use high-resolution numerical simulations to test a simple recipe for the autocovariance function of the geomagnetic coefficients based on instantaneous models of the field and its time variation. We find that the AR2 stochastic processes recently used as prior by Gillet *et al.* (2013) and Hellio *et al.* (2014) do provide an approximation of the temporal power spectra for individual Gauss coefficients in the numerical simulations. Based on these results, we argue that up to millennial periods the autocovariance function of Gauss coefficients of the actual geomagnetic field can be described with only two parameters (or three for the axial dipole).

The manuscript is organized as follows. In Section 2, we give an overview of stochastic processes that we consider in this study to model the time evolution of geomagnetic Gauss coefficients. In Section 3, we first give the main characteristics of the three different numerical dynamo simulations analysed throughout this study, before we describe the statistics (variance, correlation time and spectra) of the generated Gauss coefficients. Next, we compare the frequency spectra of non-dipole Gauss coefficients in our dynamo simulations with spectra predicted from the assumption that they are realizations of order 2 stochastic processes with a single characteristic timescale. Finally in Section 4 we describe possible deviations from spherical symmetry, and discuss the specific behaviour of the axial dipole at millennial and longer periods. Those considerations lead us to speculate about the possible mechanisms underlying the timescales of the stochastic processes that we have considered. We finally discuss consequences for uncertainty estimates in field modelling.

2 STOCHASTIC MODELS FOR THE TIME EVOLUTION OF GAUSS COEFFICIENTS

As stated by the Wiener–Khinchin theorem (Van Kampen 2007), a stationary stochastic process x of time t can be characterized either by its power spectrum $P(f)$ or by its autocovariance function $C(\tau) = E(x(t)x(t + \tau))$, where $E(\ldots)$ stands for the statistical expectation. Those two quantities are related through

$$P(f) = \int_{-\infty}^{\infty} C(\tau)e^{-i2\pi f\tau}d\tau . \tag{1}$$

We make below a connection between the stochastic processes that we use in this study and the processes that have been previously employed to model the evolution of the geocentric axial dipole.

2.1 A three-parameter AR2 process for the axial dipole

Transition between power laws $P(f) \propto f^{-4}$, f^{-2} and f^0 at respectively high, intermediate and low frequencies have been documented for the Earth magnetic field (e.g. Constable & Johnson 2005; Ziegler

et al. 2011) as well as for dynamo numerical simulations (Olson *et al.* 2012; Davies & Constable 2014; Buffett & Matsui 2015). Based on these observations, Hellio (2015) and Buffett & Matsui (2015) introduced specific stochastic processes for modelling the time changes of the axial dipole. Their two approaches are compared below.

In the following, we assume that the axial dipole coefficient samples a stochastic process $x(t)$, of non-zero average $\bar{x} = E(x)$, that is, we consider a period of constant (normal or inverse) polarity. We discuss the fluctuations $y(t) = x(t) - \bar{x}$ about this average. Hellio *et al.* (2014) proposed that y is a realization of an AR2 stochastic process, namely is solution of a differential equation of the form

$$\frac{d^2y}{dt^2} + 2\chi \frac{dy}{dt} + \omega^2 y = \zeta(t),$$ (2)

where $\zeta(t)$ is a white noise process, and the frequencies ω and χ are positive. The latter two conditions ensure that the process is stationary. For $\chi > \omega$, the frequency spectrum exhibits f^{-4}, f^{-2} and f^0 dependence at respectively high, intermediate and low frequencies. It can be expressed as (e.g. Yaglom 2004)

$$P(f) = \frac{4\chi\omega^2\sigma^2}{\left(\omega^2 - (2\pi f)^2\right)^2 + (4\pi\chi f)^2},$$ (3)

where $\sigma^2 = E(y^2)$. It is thus constrained by three quantities: the process variance σ^2, and the parameters χ and ω. The autocovariance function is given by

$$C(\tau) = \frac{\sigma^2}{2\xi}\left((\chi + \xi)e^{-(\chi-\xi)|\tau|} - (\chi - \xi)e^{-(\chi+\xi)|\tau|}\right),$$ (4)

with $\xi^2 = \chi^2 - \omega^2$. The time ω^{-1} can be obtained as the square root of the ratio between the variance of y and of its time derivative (Hellio 2015, p. 50). Indeed, the autocovariance function C is twice differentiable at $\tau = 0$, with

$$C''(0) = \left.\frac{d^2}{d\tau^2}C(\tau)\right|_{\tau=0} = -\sigma^2\omega^2,$$ (5)

and we have also (Hulot & Le Mouël 1994)

$$C''(0) = -E\left[\left(\frac{dy}{dt}(t)\right)^2\right].$$ (6)

Buffett & Matsui (2015) model instead the evolution of $x(t)$ using the stochastic equation

$$\frac{dx}{dt} = v(x) + \sqrt{D(x)}\Gamma(t),$$ (7)

where $\Gamma(t)$ is a red noise characterized by a Laplacian autocovariance function, $v(x)$ is a drift term describing the slow evolution of the axial dipole moment, and $D(x)$ defines the amplitude of random fluctuations. Following Buffett *et al.* (2013, 2014) and Buffett & Matsui (2015), the latter two terms may be approximated by $v(x) \simeq -(x - \bar{x})/\tau_s = -y/\tau_s$ and $D(x) \simeq D$, yielding a stochastic equation of the form

$$\frac{dy}{dt} + \frac{y}{\tau_s} = \epsilon(t),$$ (8)

with $\epsilon(t) = \sqrt{D}\Gamma(t)$. Since $\epsilon(t)$ is a Laplacian correlated noise, its evolution can be modelled by an order one stochastic equation of the form (e.g. Jazwinski 2007)

$$\frac{d\epsilon}{dt} + \frac{\epsilon}{\tau_f} = \zeta(t),$$ (9)

with $\zeta(t)$ a white noise process.

Combining eqs (8) and (9) leads to an equation of the form

$$\frac{d^2y}{dt^2} + \left(\frac{1}{\tau_s} + \frac{1}{\tau_f}\right)\frac{dy}{dt} + \frac{y}{\tau_s\tau_f} = \zeta(t).$$ (10)

With $2\chi = 1/\tau_s + 1/\tau_f$ and $\omega^2 = 1/(\tau_s\tau_f)$, eq. (10) defines an AR2 stochastic process similar to that defined through eq. (2). Adopting $\tau_f < \tau_s$, we obtain

$$\begin{cases} \tau_s = \dfrac{\chi + \xi}{\omega^2} \\[2mm] \tau_f = \dfrac{\chi - \xi}{\omega^2} \end{cases}.$$ (11)

For $\tau_f \ll \tau_s$, we deduce from eqs (3) and (11) that the transition period between domains of the power spectrum presenting 2 and 4 (resp. 0 and 2) spectral indices is $2\pi\tau_f$ (resp. $2\pi\tau_s$).

Hellio (2015) and Buffett *et al.* (2013) are therefore using similar stochastic models for the axial dipole. Note however that the latter implicitly states the condition ξ real and $\chi \geq \omega$ – see eq. (11). Eq. (2) is thus more general, and allows a wider range of behaviours.

2.2 A two-parameter AR2 process for non-dipole coefficients

For an AR2 process with $\chi = \omega$ (i.e. $\tau_f = \tau_s$), the frequency spectrum of the process defined from (2) is given by

$$P(f) = \frac{4\omega^3\sigma^2}{\left[\omega^2 + (2\pi f)^2\right]^2}.$$ (12)

This power spectrum is flat (spectral index $s = 0$) at low frequencies and behaves as f^{-4} for $f \gg \omega/(2\pi)$. It does not display a power law f^{-2} at intermediate frequencies. The autocovariance function of the process is given by

$$C(\tau) = \sigma^2 (1 + \omega|\tau|) e^{-\omega|\tau|}.$$ (13)

This particular autoregressive process of order 2 depends only on two parameters, the variance σ^2 and the characteristic timescale ω^{-1}. It was used by Gillet *et al.* (2013), Hellio *et al.* (2014) and Hellio (2015) to define prior information on Gauss coefficients for the computation of global archaeomagnetic and geomagnetic field models.

3 METHOD FOR CHARACTERIZING THE TIME-SPECTRA OF GAUSS COEFFICIENTS

Assuming that all Gauss coefficients but the axial dipole sample stochastic Gaussian processes of autocovariance function (13), we use numerical geodynamo simulations to discuss how to estimate the two parameters σ and ω that characterize the processes. Then, we compare the theoretical power spectrum of these processes to the actual spectrum of the Gauss coefficients in our numerical simulations.

3.1 Simulations used in the study

We rely on three dynamo numerical simulations named Step 0 (S0), Step 1 (S1) and Coupled Earth (CE). All three solve the momentum, codensity and induction equations under the Boussinesq approximation, for an electrically conducting fluid within a spherical shell of aspect ratio 0.35 between the inner core and the outer core of radius c. S0 and S1 were computed using the free XSHELLS code

Table 1. Non-dimensional numbers and timescales for numerical simulations and the Earth's core. All times are given in years. D is the shell thickness, c is the outer core radius, B and U the root mean square of the magnetic field intensity and of the velocity in the fluid shell, Ω the rotation rate, η the magnetic diffusivity, ν the kinematic viscosity, κ the thermal diffusivity, μ_0 the magnetic permeability of free space, F the mass anomaly flux at the Inner-Core boundary (chemical convection, see Aubert *et al.* 2013). C-600 and C-1400 stand for the Calypso simulations of Buffett & Matsui (2015), after translating their timescale into the τ_{SV}-based scaling used throughout this paper, with $\tau_{SV} = 14\, t_d/Rm$ (Lhuillier *et al.* 2011a). See (Backus *et al.* 1996, pp. 200–204) for the calculation of the dipole decay time t_d. †We refer to Christensen & Tilgner (2004) for the definition of the magnetic dissipation time $\tau_{\mathrm{diss}}^{\mathrm{mag}}$, ratio of magnetic energy to Ohmic dissipation. ‡The relative dipole field strength at the core surface f_{dip} is defined as in Christensen & Aubert (2006). We have adopted $\nu = 1.5 \times 10^{-6}\,\mathrm{m^2 s^{-1}}$, $\eta = 0.75\,\mathrm{m^2 s^{-1}}$, $\rho = 1.1 \times 10^4\,\mathrm{kg\,m^{-3}}$, $\tau_{SV} = 415$ yr and $B = 4 \times 10^{-3}$ T to give values for the Earth's core. The turn-over time deduced from τ_{SV} and Lhuillier *et al.* (2011a), $t_U = D/U \simeq 0.3\,\tau_{SV} \simeq 125$ yr, is consistent with $U \sim 20$ km yr^{-1} in the Earth's core and is within a factor of two of our estimates from simulations.

Name	Definition	S0	S1	CE	C-600	C-1400	Earth's core
Ekman	$E = \nu/(\Omega D^2)$	10^{-5}	10^{-6}	3×10^{-5}	5×10^{-5}	5×10^{-5}	4×10^{-15}
Flux Rayleigh	$Ra_F = FD^2/(4\pi \rho \kappa^2 \nu)$	4.4×10^{10}	8.9×10^{11}	1.0×10^9	3.1×10^7	1.5×10^8	?
Magnetic Reynolds	$Rm = UD/\eta$	710	660	940	42	90	1700
Prandtl	$Pr = \nu/\kappa$	1	1	1	1	1	0.1–10
Magnetic Prandtl	$Pm = \nu/\eta$	0.4	0.2	2.5	0.5	0.5	2×10^{-6}
Alfvén time	$t_A = D\sqrt{\mu_0 \rho}/B$	100	47	110		83	2
Dipole decay time	$t_d = c^2/(\pi^2 \eta)$	1.2×10^4	1.2×10^4	3.2×10^4	1.2×10^3	2.7×10^3	5×10^4
Turn-over time	$t_U = D/U$	69	76	140	120	120	120
Dissipation time†	$\tau_{\mathrm{diss}}^{\mathrm{mag}}$	12	14.5	41			
Dipole field strength‡	f_{dip}	0.73	0.68	0.75			0.68
Simulation duration		85×10^3	7.6×10^3	84×10^3		91×10^3	
Sampling interval		38	0.25	5.3		11	

(Schaeffer 2015), assuming no-slip and fixed homogeneous heat flux conditions at both the inner and outer boundaries. CE (Aubert *et al.* 2013) was run using the PARODY-JA code (Aubert *et al.* 2008), assuming no-slip conditions at the inner boundary, free-slip conditions at the outer core boundary, and heterogeneous mass-anomaly flux both at the inner and at the outer boundaries. This simulation also includes a gravitational coupling between the inner core and the mantle. Both codes use finite differences in radius and spherical harmonic expansion (Schaeffer 2013), together with a semi-implicit Crank–Nicolson–Adams–Bashforth time scheme of order 2.

Non-dimensional parameters and times characterizing these simulations are given in Table 1. Dimensionless times are transformed into years following Lhuillier *et al.* (2011b)—see also Sections 3.2 and 4.3. The field intensity is also rescaled to dimensional units using a proportionality constant such that the averaged root mean square (r.m.s.) field in the shell is equal to 4 mT, a value comparable to that estimated for the Earth's core by Gillet *et al.* (2010).

The longest simulations S0 and CE allow to investigate long timescales, whereas the high sampling rate and the small Ekman number in S1 give access to shorter timescales. All three simulations are dipole-dominated at the core–mantle boundary (CMB); see the relative dipole field strength f_{dip} in Table 1. They also display non-dipolar structures and significant secular variation (but no polarity reversal). The field in CE has the particularity to show prominent equatorial structures that undergo a westward drift, as observed for the Earth's magnetic field over the past four centuries (Finlay & Jackson 2003). It is also important to notice that the magnetic Reynolds number Rm (defined as the ratio of magnetic diffusion time over advection time) in our three simulations is close to the Earth's core value (see Table 1).

Statistics over periods much longer than a few 10 000 yr (e.g. involving reversals) would require much longer simulations. There is thus a trade-off between capturing the long term evolution of dipole moment changes and reproducing rapid field variations (Meduri & Wicht 2016). Robust estimates of the mean dipole field strength require simulations over many diffusion times that are presently achievable only for large Ekman number (e.g. Olson *et al.* 2012; Davies & Constable 2014). Because we are particularly interested

here into decadal to millennial timescales, we use parameters closer to (yet still far away from) the geophysical ones. Our simulations thus cover a wide range of periods shorter than the turn-over time t_U.

We show in Figs 1 and 2 examples of the time-series that we analyse in the rest of the paper. The axial dipole has a non-zero mean value and displays large long-period fluctuations. We observe a decrease of both the amplitude and the timescale of fluctuations of the other coefficients with degree. While temporal fluctuations of all coefficients seem rather stationary in simulations S0 and CE (Fig. 1), non-stationarity is observed in the shorter simulation S1 for the largest degrees (Fig. 2, right). Note that periodic oscillations are observed for coefficient $\mathcal{G}_2^1$ in CE. These oscillations will be discussed in Section 4.2.

3.2 Variance and correlation time of Gauss coefficients

The magnetic field **B** outside the core is described through a scalar potential V such that $\mathbf{B} = -\nabla V$. In this work, Gauss coefficients $\mathcal{G}_n^m$ and $\mathcal{H}_n^m$ are defined at the core surface (and not at the Earth's surface) with n and m the spherical harmonics degree and order, N the truncation degree, hence V is decomposed as

$$V(r, \theta, \phi, t) = c \sum_{n=1}^{N} \left(\frac{c}{r}\right)^{n+1} \sum_{m=0}^{n} \left(\mathcal{G}_n^m(t) \cos m\phi + \mathcal{H}_n^m(t) \sin m\phi\right) P_n^m(\cos\theta), \tag{14}$$

where r is the distance to the Earth centre, θ the colatitude, ϕ the longitude and P_n^m are the Schmidt quasi-normalized Legendre functions. We define the spatial power spectra for the geomagnetic field and its secular variation

$$\begin{cases} R_n = (n+1) \sum_{m=0}^{n} \left[E\left(\mathcal{G}_n^{m\,2}\right) + E\left(\mathcal{H}_n^{m\,2}\right)\right] \\ \\ S_n = (n+1) \sum_{m=0}^{n} \left[E\left(\partial_t \mathcal{G}_n^{m\,2}\right) + E\left(\partial_t \mathcal{H}_n^{m\,2}\right)\right] \end{cases} \tag{15}$$
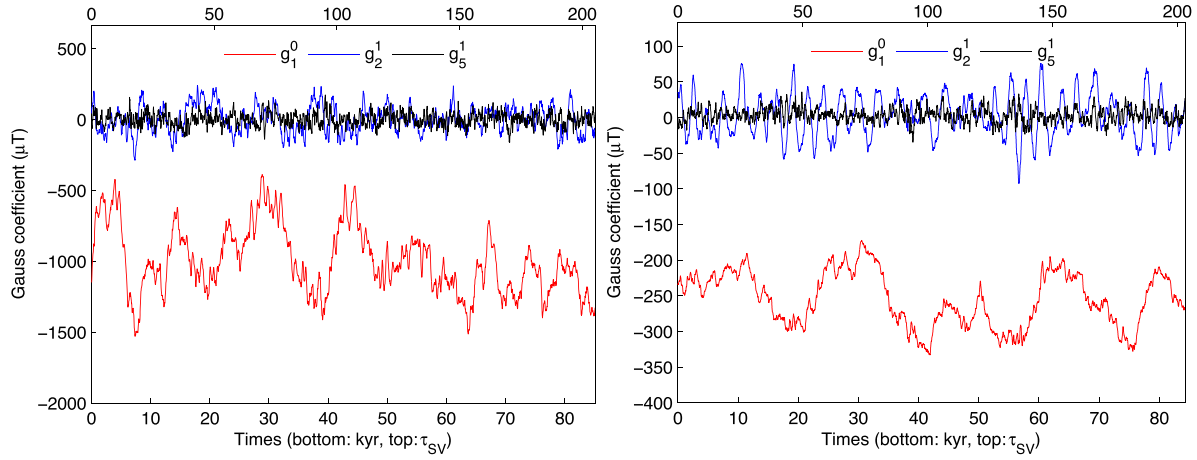
Figure 1. Time-series of coefficients $\mathcal{G}_1^0$, $\mathcal{G}_2^1$ and $\mathcal{G}_5^1$ from simulations S0 (left) and CE (right). The top scale gives the dimensionless time (based on τ_{SV}).
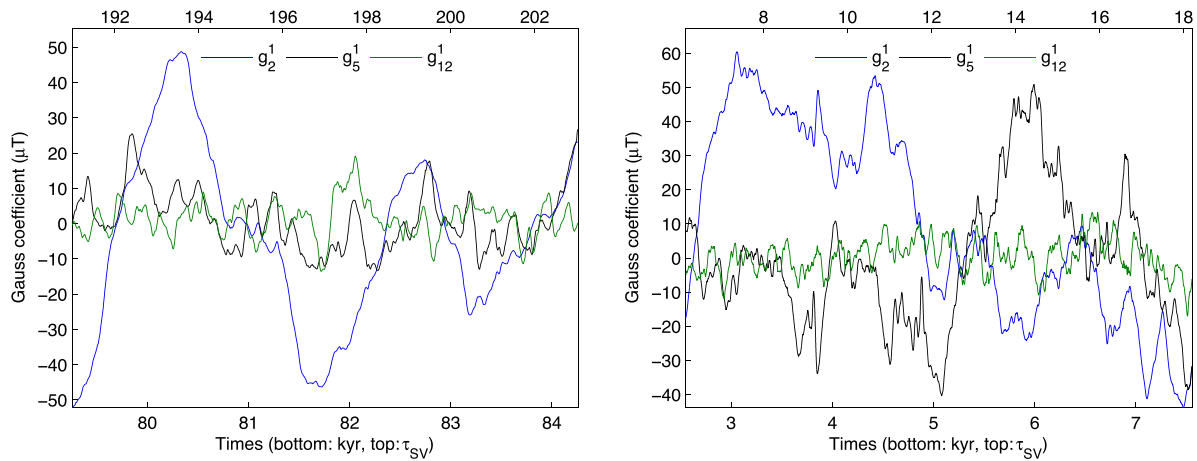
Figure 2. 5 kyr time-series of coefficients $\mathcal{G}_2^1$, $\mathcal{G}_5^1$ and $\mathcal{G}_{12}^1$ from simulations CE (left) and S1 (right). The top scale gives the dimensionless time (based on τ_{SV}).

as functions of degree n, from which a correlation time $\tau_n = \sqrt{R_n/S_n}$ can be derived (Hulot & Le Mouël 1994).

The two quantities R_n and τ_n are now assumed to follow simple laws as a function of the degree n (for $n \geq 2$):

$$R_n \simeq \alpha\beta^n, \qquad \tau_n \simeq \delta n^{-\gamma}. \qquad (16)$$

Constable & Parker (1988b) found that geomagnetic field models ($1 \leq n \leq 12$) are consistent with $\beta = 1$, whereas Roberts *et al.* (2003) inferred $\beta \simeq 0.90$ from observations for $n \geq 3$. Holme & Olsen (2006) and Lesur *et al.* (2008) examined their satellite field models and estimated $\gamma \simeq 1.45$ and $\gamma \simeq 1.375$ respectively whereas Christensen & Tilgner (2004) and Lhuillier *et al.* (2011b) argued instead for $\gamma = 1$ in joint analyses of geodynamo simulations and geomagnetic field models. The latter authors also scaled time in simulations so that $\tau_{SV} = \delta|_{\gamma=1}$ matches the geophysical value and estimated $\tau_{SV} = 415$ yr from a fit of τ_n for degrees $n \in [2-13]$.

Building on these works, we shall assume $\beta = \gamma = 1$ hence a flat spatial power spectrum R_n at the CMB for the observable length-scales. This simplification allows to easily convert numerical times into years. The remaining parameters (α, δ) entering eq. (16) can be derived from the average of R_n and a least-squares fit of $\log(\tau_n)$ versus $\log(n)$. Since these two quantities are not normally distributed, a more accurate estimate may be obtained using a maximum likelihood approach, as developed by Lhuillier *et al.* (2011b) for τ_n (see Appendix A). We discuss in Appendix B the estimation

of the parameters of the regression model (16) as the conditions $\beta = \gamma = 1$ are relaxed.

For each simulation, we have computed different estimates of the spatial power spectrum R_n and of the time τ_n: an ensemble of instantaneous values $(\hat{R}_n, \hat{\tau}_n)$ averaged over m ($0 \leq m \leq n$) only, an estimate $(\overline{R}_n, \overline{\tau}_n)$ averaged over m and the total duration of the simulations, and the similarly averaged (R_n^*, τ_n^*) once subtracted the mean values of the coefficients. Time-averaged estimates $(\overline{R}_n, \overline{\tau}_n \times n)$ and $(R_n^*, \tau_n^* \times n)$ are shown in Fig. 3 for the three simulations. We also represent the fits $R_n = \alpha$ and $\tau_n \times n = \delta$ calculated either with the least-square method or the maximum likelihood one. In addition, we plot two-sigma intervals for α and δ deduced from an ensemble of ten snapshots. Overall, the different time-averaged estimates of α and δ yield rather similar results given the large variability within the ensemble of snapshot estimates. Removing or not the average appears therefore as a secondary issue.

Spectra R_n for CE and S0 simulations are almost flat, validating the hypothesis $\beta = 1$, while that for the most extreme (lowest viscosity, strongest forcing) simulation S1 presents a slightly decreasing trend with n, closer to current estimates from geomagnetic field models, as further discussed in Appendix B.

Times τ_n reflect slightly different behaviours in all three simulations. If the hypothesis $\gamma = 1$ agrees well with the outputs from CE, S1 (resp. S0) favours instead a slightly larger (resp. lower) exponent. In simulation S1, we obtain a γ value closer to 1 after removing the time-average value of the coefficients, which mainly
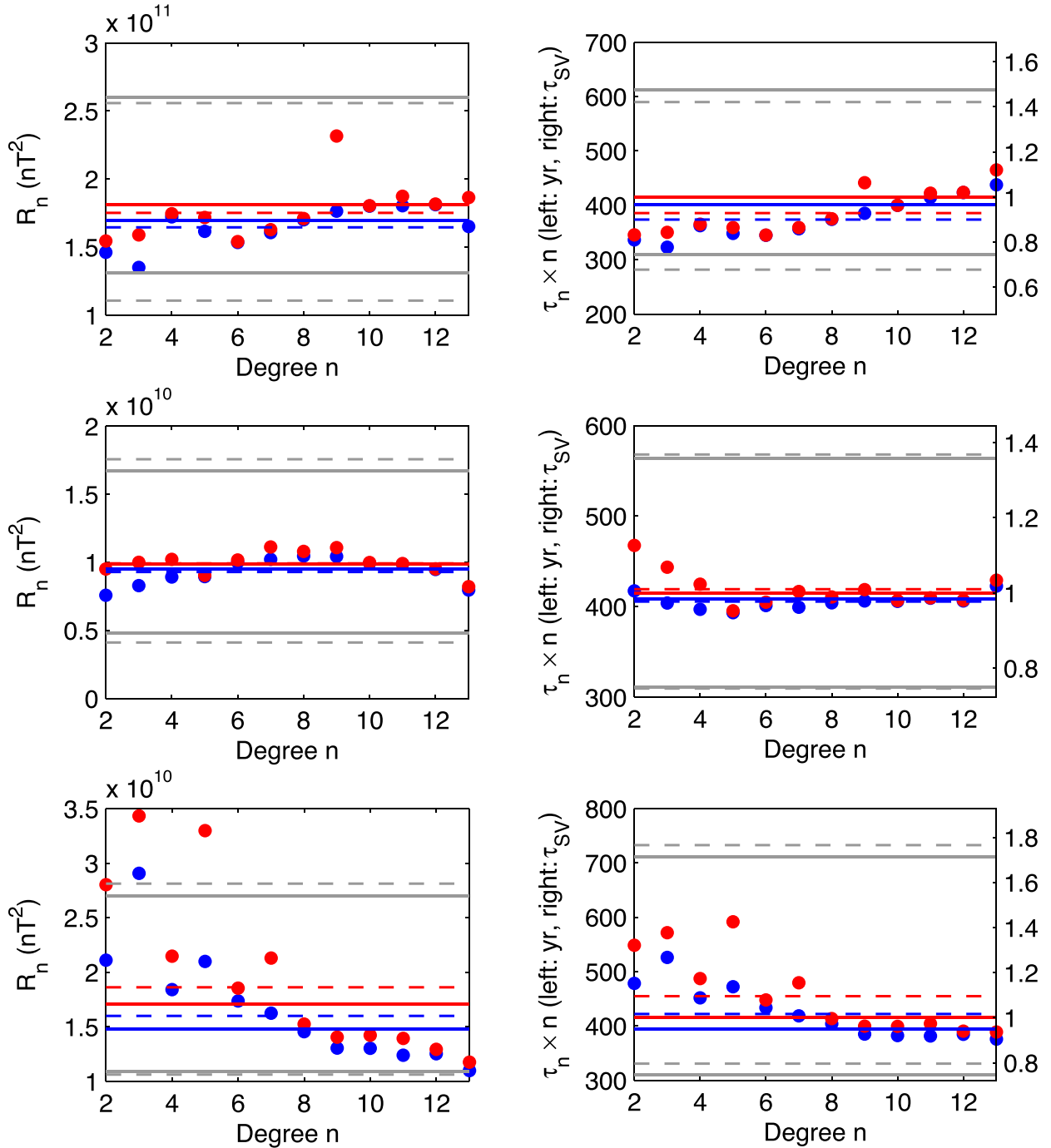
Figure 3. Spatial power spectrum R_n (left) and $n \times \tau_n$ (right) as a function of the spherical harmonic degree n for simulations S0 (top), CE (middle) and S1 (bottom) from the expected variances as in eq. (15), either removing (blue dots) or keeping (red dots) the time-average of the coefficients. Dashed (resp. solid) coloured lines stand for estimates of α and δ using least-squares (resp. maximum likelihood) regressions (16) with $\beta = \gamma = 1$. Grey lines represent the two-sigma intervals around the average of 10 estimates of α and δ from independent snapshots $\hat{R}_n$ and $\hat{\tau}_n$, which are not represented. The right scale on the $n \times \tau_n$ plots gives the dimensionless time in τ_{SV} units.

affects τ_n estimates at low degrees. Furthermore, we note a wide time variability in the instantaneous estimates $\hat{\tau}_n$, suggesting that a snapshot estimate alone, as available from modern geophysical observations (see e.g. Holme *et al.* 2011) for which the long-term average of coefficients is not available, is insufficient to determine precisely γ. All in all, we conclude that the simple hypothesis $\gamma = 1$ is consistent with our three simulations (see Appendix B for more details). An error of the order of 50 per cent may occur when

measuring the magnitudes of α and δ from instantaneous values, as shown by the two-sigma interval in Fig. 3 (right) and in Table B2. This translates into a variability in τ_{SV} significantly larger than that observed by Lhuillier *et al.* (2011b) from a dynamo simulation at larger viscosity and lower forcing.

Note that the time-series of non-dipole coefficients represented on Fig. 2 appear uncorrelated when sampled over periods longer than $2\pi \tau_n = 2\pi \tau_{SV}/n$ (i.e. for periods longer than about 1300, 500
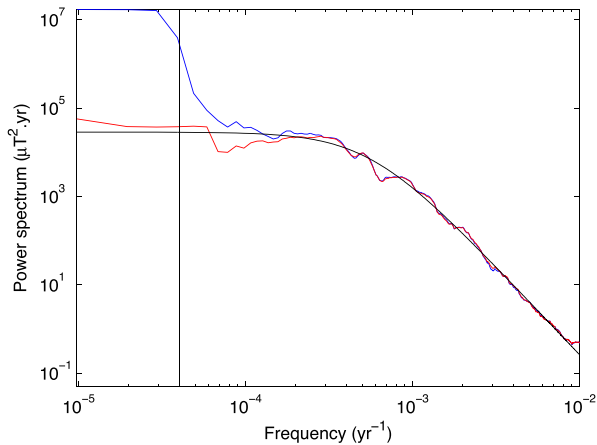
Figure 4. Comparison of power spectra for random time-series, estimated using the multitaper approach applied before (blue) and after (red) removing the averaged value of the series, and superimposed on the theoretical power spectrum (black). The series parameters are chosen to mimic a plausible behaviour for the axial dipole coefficient (at the Earth's surface): it is a Gaussian random series with an averaged value of -35 μT, a standard deviation of 5 μT, with a two-parameters AR2 autocovariance function as defined in eq. (13), with $\omega^{-1} = 500$ yr. The theoretical power spectra of this series are given in eq. (12). The series contains $N = 2000$ data sampled every $\Delta t = 50$ yr. The vertical black line indicates the value of the concentration half-bandwidth $W = 4/(N\Delta t)$ of the Slepian tapers. These spectra were obtained using the subroutine pmtm from Matlab and then further smoothed using running averages.

and 200 yr for degrees 2, 5 and 12 respectively). This suggests a flat power spectrum at lower frequencies, as expected for the two-parameter AR2 processes described in Section 2.2.

3.3 Frequency spectra of Gauss coefficients

In order to avoid frequency leakage when estimating the power spectrum for the finite-length time-series of Gauss coefficients, we adopt a multitaper approach (e.g. Percival & Walden 1993). The advantage of this approach is that the power spectrum variance is reduced by averaging independent estimates of the power spectrum obtained after multiplying the series by various orthogonal tapers. Several variants of the multitaper approach have been used before to assess the power spectrum of the dipole moment. Constable & Johnson (2005) relied on sine tapers (Riedel & Sidorenko 1995). Olson *et al.* (2012) chose instead to break the series into overlapping segments tapered using a Hanning window (Welch 1967). As Buffett & Matsui (2015), we adopt in this study an approach based on Slepian functions (Thomson 1982). We use seven Slepian tapers characterized by a power spectrum with energy concentrated in a bandwidth $[-W, W]$, where $W = 4/(N\Delta t)$, N is the number of data, and Δt is the sampling interval. As a consequence, the power spectrum estimated at a given frequency f is controlled by values of the power spectrum within $[f - W, f + W]$, with W the resolution of the power spectrum.

We test the multitaper approach of Thomson (1982) on a realization of a stochastic process. The obtained spectra are further smoothed by running averages over a length that linearly increases with the frequency (from 1 point at minimum frequency to 201 points at maximum frequency). We show the spectra obtained for this realization both before and after removing its averaged value (Fig. 4). Although these power spectra include a certain amount of noise, they reproduce well both the amplitude and the spectral

indices of the true power spectrum, except at frequencies lower than the resolution W. At frequencies $f < W$, the average value of the series influences the power spectra, which strongly differ whether the average is removed or not: the spectrum obtained without removing the average shows a step at low frequencies, which is an artefact. The above method for calculating spectra is used below for all our results. Note that we do not remove linear trends in the time-series before computing the spectra. Nevertheless, we checked that the shape of the spectra computed here with the multitaper approach is not significantly different whether the trend has been removed or not.

Fig. 5 displays power spectra for degree 5 Gauss coefficient time-series at the CMB, from the three simulations. For the two longest simulations (S0 and CE), we observe that spectra for all coefficients are flat (or white) at low frequencies, and show a constant spectral index at high frequencies, hinting to a scale invariance. The change of spectral index occurs within a narrow band of frequencies, and the cut-off frequency between the two regions of the spectra increases with the spherical harmonic degree, as illustrated in Fig. 6 for the CE dynamo. Whereas the spectral index at large frequencies appears independent of the spherical harmonic order in S0, it significantly increases with m in the CE and S1 simulations. Power spectra obtained from S1 do not show a flat plateau at low frequencies as a consequence of the short duration of the simulation: we do not have access to long enough periods to reach the domain where $P \propto f^0$. Spectra for this simulation show a steep decrease with f at high frequency, which is absent in the S0 and CE spectra.

3.4 Comparison with the spectrum of a two-parameter AR2 process

Expression (13) corresponds to a particular autoregressive process of order 2 that only depends on two parameters, a variance σ^2 and a characteristic timescale ω^{-1}. As in Gillet *et al.* (2013), we further assume that these two parameters only depend on the spherical harmonic degree n, which amounts to posit that the statistics of the field are independent of longitude and latitude (Hulot & Bouligand 2005). Then, for each degree n, one deduces from (15) that $\sigma_n^2 = R_n/(n + 1)(2n + 1)$, and from eqs (5) and (6) the relation $\omega_n^{-1} = \tau_n$; these two parameters define the autocovariance functions $C_n(\tau)$.

Since long enough geophysical series to produce statistical averages are not available, Gillet *et al.* (2013) approximated (R_n, τ_n) by the quantity $(\hat{R}_n, \hat{\tau}_n)$ estimated from a snapshot of the well documented (and supposedly representative) satellite era. This approximation relies on the assumption that main field and secular variation series are unbiased, that is, $E(\mathcal{G}_n^m) = E(\mathcal{H}_n^m) = E(\partial_t \mathcal{G}_n^m) = E(\partial_t \mathcal{H}_n^m) = 0$. This assumption is certainly not valid for the axial dipole between two polarity reversals. For this reason, Hellio *et al.* (2014) considered instead dipole deviations in the expression (15) for $n = 1$. We test here the validity of using snapshot estimate $(\hat{R}_n, \hat{\tau}_n)$ to define the autocovariance function of non-dipole coefficients.

For each simulation, we estimate parameters α and δ entering (16) (with $\beta = \gamma = 1$) using both averaged and instantaneous estimates of the spatial power spectrum and correlation times (i.e. $(\bar{R}_n, \bar{\tau}_n)$, (R_n^*, τ_n^*) and $(\hat{R}_n, \hat{\tau}_n)$) and a maximum likelihood approach. α and δ are then used to determine variances σ_n^2 and correlation times ω_n^{-1}, and to predict the theoretical spectrum (12) for all degrees n. We then estimate a two-sigma interval from 10 spectra (12) deduced from snapshots. These curves are superimposed in Fig. 5 (for
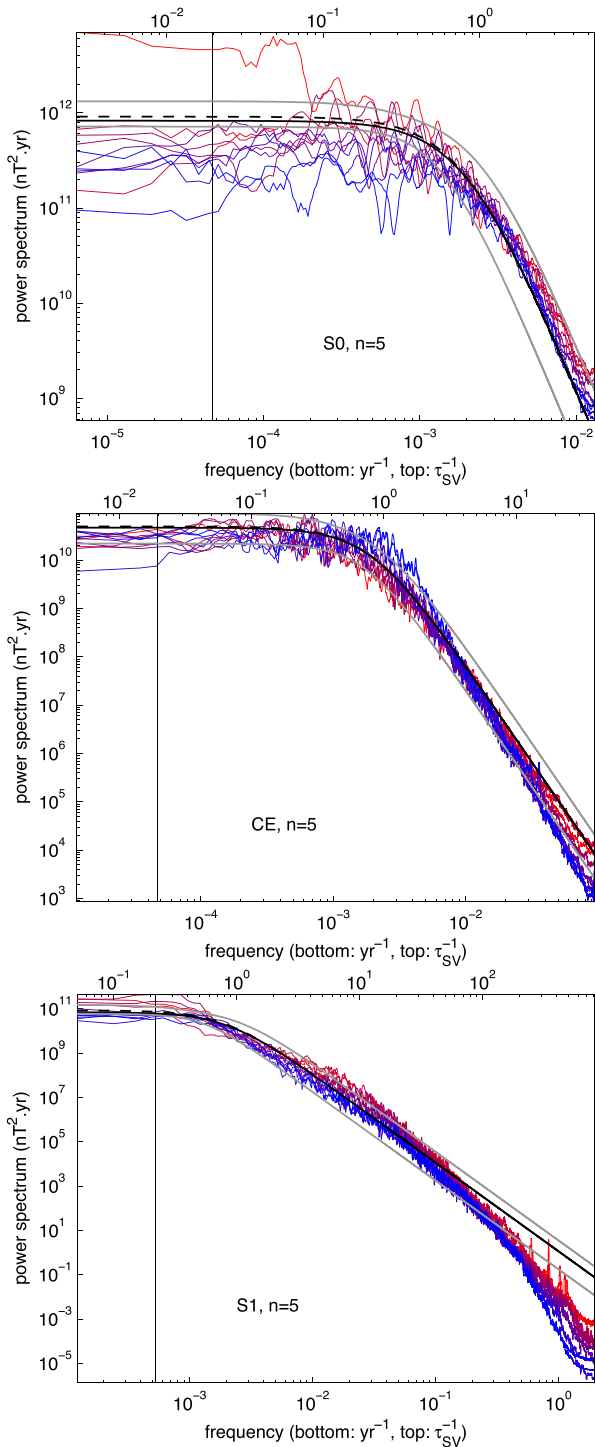
Figure 5. Power spectra computed using the multitaper approach of Thomson (1982) for coefficients of degree $n = 5$, from simulations S0 (top), CE (middle) and S1 (bottom). All coefficients $\mathcal{G}_n^m$ and $\mathcal{H}_n^m$ of order $m \in [0, n]$ are represented with gradually varying colours (from red for $m = 0$ to blue for $m = n$). The black solid (dashed) curves display the power spectra (12) with parameters τ_n and σ_n estimated using the maximum likelihood method and using time averaged Gauss coefficients variances in eq. (15), once removed (or not) their averaged value. The grey lines represent the two-sigma interval around the average of 10 power spectra with parameters ω_n^{-1} and σ_n deduced from independent snapshot $\hat{R}_n$ and $\hat{\tau}_n$. The thin vertical black line indicates the resolution half-bandwidth. The top scale gives the dimensionless frequency (based on τ_{SV}^{-1}).
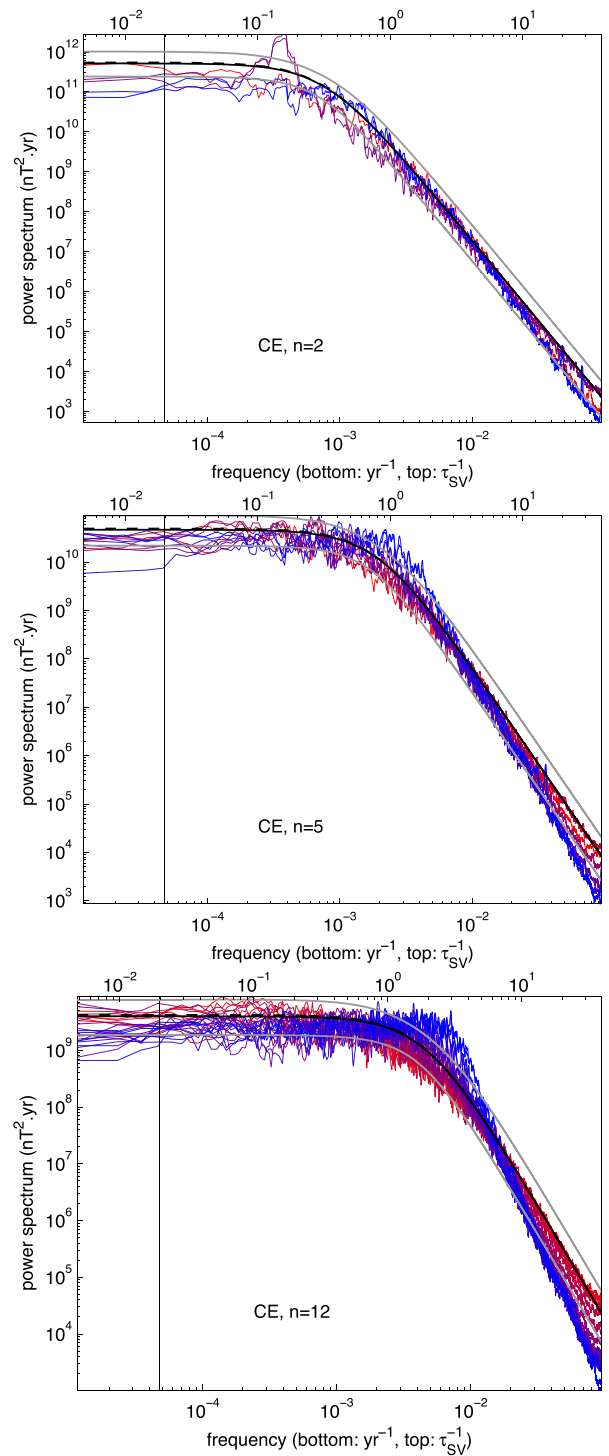
Figure 6. Power spectra for Gauss coefficients series of spherical harmonic degrees 2, 5 and 12, from the CE simulation. Same colours and line types as in Fig. 5.

$n = 5$) and Fig. 6 (CE simulation for $n = 2, 5, 12$) on spectra of the Gauss coefficients.

For all three simulations and all degrees, we observe overall a good agreement between the different theoretical spectra, with some discrepancies that we detail in the next paragraph. The theoretical spectra obtained from averaged estimates, once removed or not the coefficient averaged value, are very close, suggesting that the assumption of unbiased series is valid. The two-sigma intervals
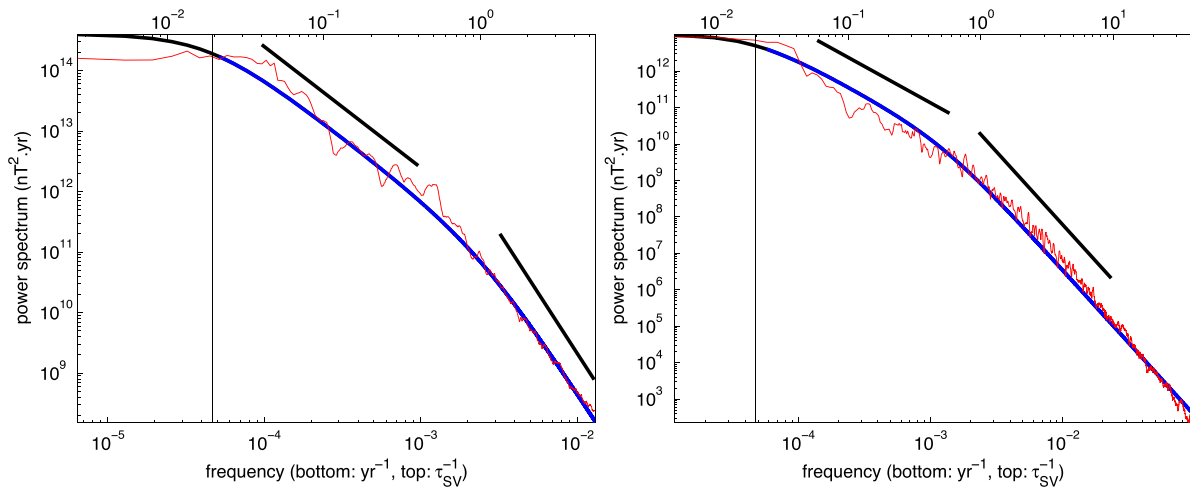
Figure 7. Power spectra (red) for the axial dipole series from simulations S0 (left) and CE (right). In black are superimposed the three parameters AR2 spectra (3) fitted to the series spectra for $f > W$ – range covered by the blue fit. The parameter W denotes the resolution half-bandwidth. The axial dipole variance is obtained directly from the series (removing the average). The frequency ω is estimated from the square root of the ratio of the variances of $\mathcal{G}_1^0$ and $\partial \mathcal{G}_1^0 / \partial t$. The remaining parameter χ is obtained by minimizing the L2 norm of the difference between the logarithms of $\mathcal{G}_1^0$ series spectrum and of eq. (3). The top scale gives the dimensionless frequency (based on τ_{SV}^{-1}). The thin vertical line indicates $f = W$. Black segments indicate spectral indices of 2 and 4.

are relatively narrow compared to the noise level in the individual spectra and to the variability among spectra of same degree, showing that the use of snapshot estimates is appropriate.

For simulation S0, the power-spectra calculated from (12) reproduce very well the power spectra of the field coefficients at all frequencies. For simulation CE, the spectrum (12) approximates relatively well the power spectra of low order Gauss coefficients for all degrees n. On the other hand, the power spectra for the largest order coefficients ($m \sim n$) decreases more rapidly than f^{-4} at its high frequency end. Simulation S1 also presents, at periods shorter than 10 yr, Gauss coefficient power spectra steeper than f^{-4}. Buffett & Matsui (2015) conjecture that the occurrence of a period range presenting a $s = 6$ spectral index, as observed from numerical computations (Olson *et al.* 2012; Davies & Constable 2014), could be related with a mechanism involving magnetic diffusion below the CMB. However, the identification of a spectral index s requires a power-law behaviour $P(f) \propto f^{-s}$ over a significant frequency range. Instead, a power spectrum $P(f) \propto \exp(-f)$, which is reminiscent of a dissipation range (see e.g. Frisch 1995), may arguably be observed at high frequencies in simulation S1. Hence, the narrow range of frequencies that displays a spectral index of 4 may result from too important diffusive processes in simulations (see Section 4.3).

4 DISCUSSION

4.1 Model for dipole fluctuations

The minimal model (12), which appears appropriate for all Gauss coefficients but the axial dipole in our simulations, involves only one timescale ω^{-1}. It can be presented (see Section 2.1) as a special case ($\omega = \chi$, i.e. $\tau_s = \tau_f$) within a more general family of models (3) having two distinct timescales ω^{-1} and χ^{-1} – or equivalently τ_s and τ_f, see eq. (11). For $\omega < \chi$, the associated power spectra (3) show a power law in f^{-2} at intermediate frequencies – between frequencies $1/(2\pi\tau_s)$ and $1/(2\pi\tau_f)$. For this reason, they were employed by Buffett & Matsui (2015) to account for the spectrum of the axial dipole as inferred from numerical simulations and from geomagnetic models. We concur with these results. In the two simulations

S0 and CE that are long enough to address long-lived dipole fluctuations, the power spectrum for the axial dipole coefficient $\mathcal{G}_1^0$ does not present a sharp transition from 0 to 4 spectral index (see Fig. 7). Contrary to the equatorial dipole coefficients $\mathcal{G}_1^1$ and $\mathcal{H}_1^1$, whose spectra are well fitted by a two parameters AR2 spectrum (12), the spectrum for $\mathcal{G}_1^0$ shows an intermediate spectral index over about one decade, which is well fitted by the three parameter function (3).

The calculation of τ_s and τ_f by Buffett & Matsui hinges on the determination of the two transition frequencies between domains of spectral index 4, 2 and 0, respectively (see Section 2.1). Fig. 7 illustrates our fit between the spectra for S0 and CE and the function (3) where we have entered our estimations for ω and χ (directly related to τ_s and τ_f). Table 2 gives a comparison between our results and the values of τ_s and τ_f calculated by Buffett & Matsui but scaled in units of τ_{SV}. In S0 and CE, the transition frequency between domains of spectral index $s \simeq 2$ and $s \simeq 4$ (Fig. 7) leads to $\tau_f \simeq 65$ and 125 yrs respectively, values about two to three times larger than the estimates by Buffett & Matsui. Switching to long periods, they made the analogy between the times τ_s and t_d found in their simulations. Although this analogy cannot be ruled out by our results, simulations S0 and CE show values of the ratio t_d/τ_s significantly different from 1 (see Tables 1 and 2).

Unfortunately, the frequency range with a flat power spectrum is clear neither in the simulations investigated here, nor in those of Buffett & Matsui. In both studies, this part of the power spectrum is within the concentration bandwidth of the taper (see their fig. 4 and our Fig. 7); we thus cannot determine if this is to be associated with a real feature of the axial dipole power spectrum, or with an artefact due to tapering. As a result, the estimates of τ_s obtained from numerical simulations and given in Table 2 are not very accurate. Nevertheless, all estimates for $\omega^{-1} = (\tau_s \tau_f)^{1/2}$ obtained from numerical series of the axial dipole are within a factor of 2 of the value that we would obtain by extrapolating the relation $\omega_n^{-1} = \tau_n = \tau_{SV}/n$ (used for non-dipole coefficients) to the degree $n = 1$ (i.e. $\omega^{-1} = 415$ yr).

The time ω^{-1} inferred from palaeo- and archaeomagnetic models appears significantly longer than estimates deduced from numerical simulations. In our opinion, the spectra of archaeomagnetic field models, in the high frequency range where the spectral index is $s \simeq 4$,

Table 2. Timescales τ_s and τ_f involved to reproduce the power spectrum of the axial dipole deduced from archaeo- and palaeomagnetic observations and from dynamo numerical simulations [see the definitions of τ_s and τ_f in eqs (8) and (9), respectively]. The time ω^{-1} is obtained as $(\tau_s \tau_f)^{1/2}$. The different times of the Calypso simulations have been converted into the τ_{SV}-based scaling adopted throughout the paper, using $t_d = Rm \times \tau_{SV}/14$ (Lhuillier *et al.* 2011a). [†1] Ziegler *et al.* (2011), [†2] Korte & Constable (2011).

Model/Simulation	τ_s (yr)	τ_f (yr)	ω^{-1} (yr)	Reference
PADM2M[†1] - CALS10k.1b[†2]	29 000	100–200	1700–2400	Buffett *et al.* (2013); Buffett & Matsui (2015)
Calypso (Rm=90)	1050	37	200	Buffett *et al.* (2014); Buffett & Matsui (2015)
Calypso (Rm=42)	1100	35	200	Buffett & Matsui (2015)
S0	3610	65	480	
CE	3490	125	660	
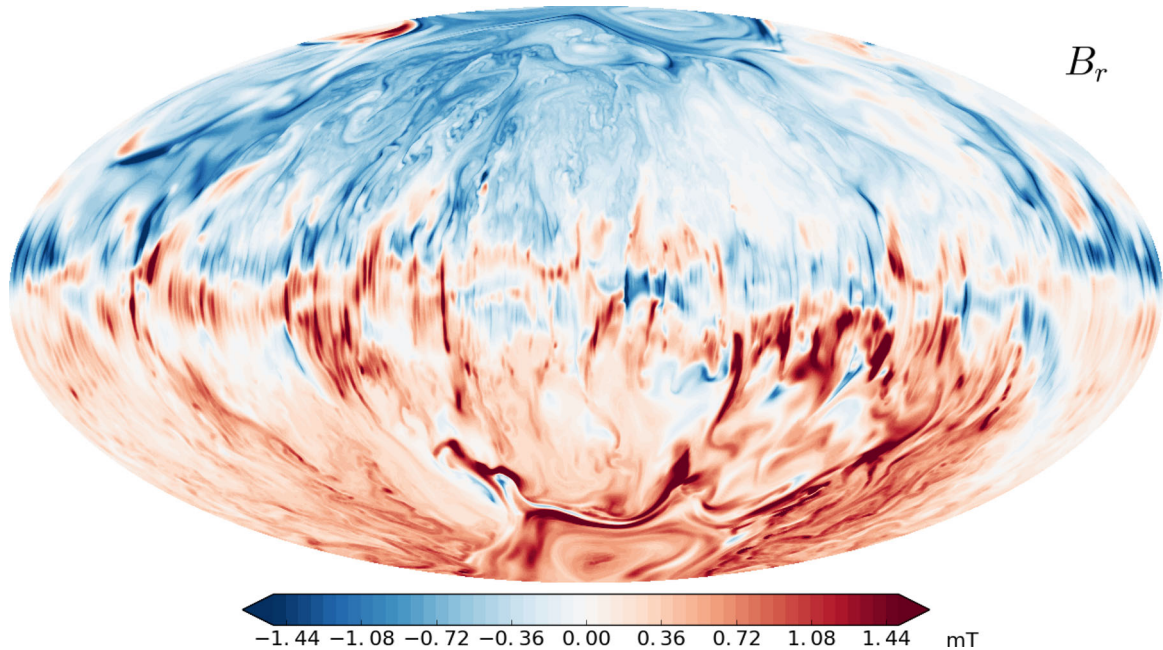
Figure 8. Full resolution snapshot of the radial magnetic field at the CMB for the S1 simulation, shown using an Aitoff projection. In this snapshot, the maximum intensity of the magnetic field at the CMB is about 7 mT.

are much influenced by the regularization used in their construction. This explains why these models do not resolve geomagnetic jerks.

4.2 Deviations from spherical symmetry

Whereas temporal spectra from simulation S0 are fairly independent of the order m for all degrees but $n = 1$ (Fig. 5), suggesting that fluctuations of the non-dipole field are spherically symmetric at the CMB, we detect some significant dependence on the order from computations CE and S1. In CE, the spectra for coefficients of large order ($m \simeq n$) present a larger spectral index at high frequencies. As a consequence, more energy is contained in coefficients of small order at high frequencies and in coefficients of large order at intermediate frequencies (for periods typically from 100 to 1000 yr). Because spherical harmonics of low and large orders have their largest contributions at respectively high and low latitudes, this suggests fluctuations at intermediate periods are stronger at low latitude (equatorial features primarily project into sectorial coefficients). This likely reflects the westward drift of low latitude structures observed in the CE simulation (see Aubert *et al.* 2013).

The power spectra for coefficients $\mathcal{G}_2^1$ and $\mathcal{H}_2^1$ in simulation CE (and to a lesser extent for order 1, degrees 4 and 6 coefficients, not shown) display a significant peak at periods around 2500 yr (see Fig. 6), which translates into quasi-periodic oscillations in the time-series (see Fig. 1, right). This particular period corresponds to the time needed to circumnavigate the outer core at the average speed of the westward drift (Aubert *et al.* 2013). These periodic variations mainly affect $m = 1$ coefficients of the magnetic field through the advection of the eccentric gyre resulting, in the CE scenario, from the heterogeneous heat fluxes.

The topology of field patches at the CMB is influenced by the underlying dynamics. Indeed, the predominant Coriolis force in geodynamo simulations favours columnar structures aligned with the rotation axis, and together with magnetic forces it textures the vorticity field in the equatorial plane (e.g. Kageyama *et al.* 2008). As a result of field concentration by the vortices, the magnetic field at the CMB (outside the polar caps above and below the inner core) shows thin filaments primarily aligned along meridians (e.g. Takahashi & Shimizu 2012). This is illustrated in Fig. 8 for our lowest viscosity case, the strongly forced computation S1. We have thus some evidence that the Gauss coefficients at the core surface cannot be treated as independent variables.

We deduce the following consequences for the inversion of geomagnetic data. First, using an AR2 autocorrelation function that is independent of the coefficient order as prior information for the inversion of geomagnetic models may penalize actual features of the geomagnetic field such as the westward drift of equatorial flux patches (Finlay & Jackson 2003) or periodic signals. Second, accounting for spatial cross-covariances (as performed with twin
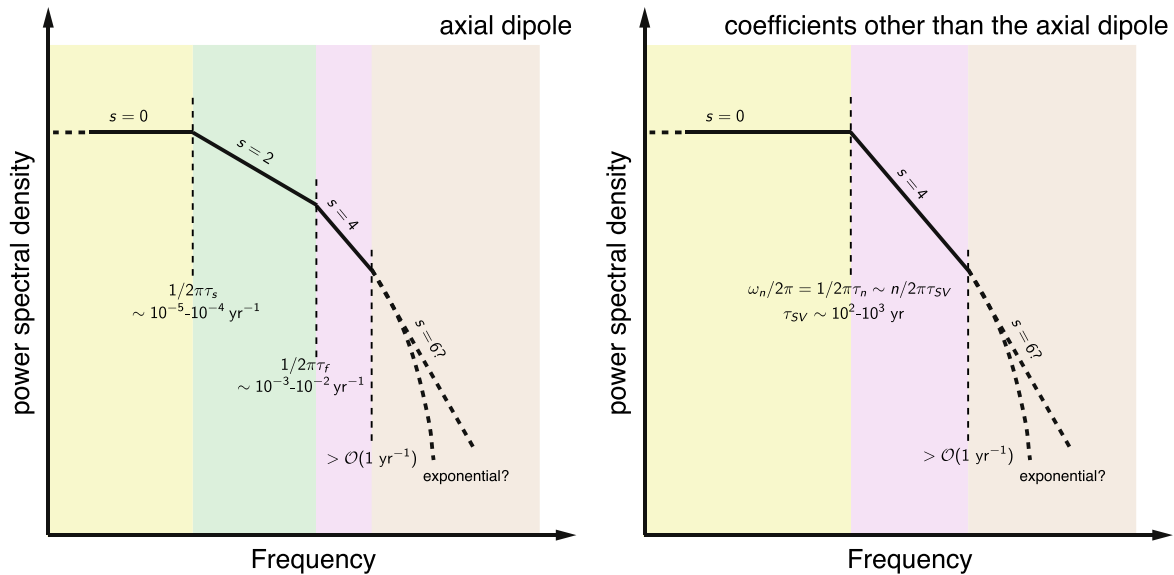
Figure 9. Schematic view of the power spectrum for the axial dipole (left) and non-dipole (right) coefficients. We associate the cut-off frequencies between domains of different spectral indices to several typical timescales. Note that there is a factor of 2π between the cut-off periods in the power spectra and the timescales τ_s and τ_f of eq. (11).

experiments on geodynamo simulations by Fournier *et al.* 2013) may improve the construction of prior information in field modelling studies.

4.3 Mechanisms underlying the different timescales

Our approximation for the spectra of all coefficients but the axial dipole involves only one timescale ω_n^{-1} $(=\tau_{SV}/n)$. Lhuillier *et al.* (2011a) argued that τ_{SV} is related to the advection time t_U, $\tau_{SV} \simeq 3t_U \simeq 14t_d/Rm$ (see Table 1 for definitions) and this relationship holds within a factor of 2 in our simulations. This link between τ_{SV} and t_U suggests that the advection time, or eddy turnover time, controls the times ω_n^{-1}.

Our observation, from simulations S0 and CE, of a sharp transition between 0 and 4 spectral index ranges suggests that fluctuations of non-dipole coefficients are controlled by a single timescale, or by two timescales that are not significantly different. In our simulations, the axial dipole is the only coefficient for which we found necessary to consider AR2 processes defined with two distinct timescales in order to account for the existence of a frequency range displaying a spectral index of 2. One could wonder as Buffett *et al.* (2013) whether this is to be related to the specificity of the axial dipole to show a non-zero average value. However, in this regard, our simulations may not be representative of the Earth magnetic field. Indeed, differences between timescales are smaller in simulations than they are for the Earth's core (see Table 1). In particular the ratio between the Alfvén time and the vortex turn-over time is about unity in simulations, instead of 10^{-2} in the Earth's core, which potentially shrinks the dynamics at periods between a few years and a few centuries in numerical computations. Therefore, if two timescales were involved in the fluctuations of the Earth non dipole coefficients, these timescales may be too close in simulations to be clearly distinguished. Relatively larger magnetic energy (and thus shorter Alfvén time) can be achieved in computations at Pm larger than unity (see e.g. Dormy 2016). Such computations unfortunately tend, at low Ekman numbers, to produce dynamos with Rm significantly lower than that of the Earth.

The simulation S1 covers a higher frequency range than S0 and CE. In this simulation, we observe that the spectrum becomes steeper than f^{-4} at periods shorter than a cut-off period $2\pi\tau \sim 3$ yr (see Fig. 5 bottom). From the inspection of other spectra ($n \neq 5$, not shown), we find no evidence of the dependence of this cut-off time on the degree. Olson *et al.* (2012) also suggested, from dynamo simulations, a transition at high frequency towards a f^{-6} dependence in the axial dipole spectrum. They attributed this transition to the damping effect of the viscous layer beneath the outer boundary. Following these authors and interpreting the time τ as a magnetic dissipation time through a surface layer of thickness ϵ, that is, $\tau = \epsilon^2/\eta = \pi^2 t_d \epsilon^2/c^2$, we find $\epsilon \sim 2 \times 10^{-3}c$. As a result, the thickness of the dissipative layer ϵ is found to be about three times the Ekman layer thickness, $E^{1/2}D$ (e.g. Greenspan 1968). Simulations differ from the geophysical situation inasmuch they are controlled by viscosity (Soderlund *et al.* 2012; King & Buffett 2013; Cheng & Aurnou 2016), with length-scales for viscous and magnetic dissipation being comparable. In a more Earth-like regime where viscosity is negligible, we can expect a dissipation cut-off at higher frequency associated to a thinner dissipative layer. We have indeed no evidence of a cut-off period from geomagnetic observations (Finlay *et al.* 2013).

4.4 Concluding remarks

The two sketches presented in Fig. 9 summarize our interpretation of the coefficients power spectra, relating the cut-off periods between domains with different spectral indices to several characteristic timescales.

The analysis of our simulations indicates that the spectra of simple two-parameters AR2 processes, calibrated by instantaneous values of R_n and τ_n, provide a good approximation of the spectra of all individual Gauss coefficients but the axial dipole. Although the axial dipole requires a more sophisticated AR2 process to account for the spectral index of 2 observed at millennial and longer periods, the use of a two-parameter process may still be sufficient for the construction of geomagnetic models. Indeed, prior information

is mainly needed to quantify the high frequency variability of the coefficients (Hellio *et al.* 2014). In particular, the axial dipole being well constrained by measurements, the behaviour of its prior at low frequency does not matter much.

Previous to this work, it was already known that there is a good agreement for the spectrum of the axial dipole between simulations and observations (Buffett & Matsui 2015). Assuming that this correspondence holds for the other field coefficients, we end up with a prescription for the prior needed to model the observed field, namely the covariance function (13) in the non-dipolar case.

ACKNOWLEDGEMENTS

REFERENCES

Aubert, J., 2015. Geomagnetic forecasts driven by thermal wind dynamics in the Earth's core, *Geophys. J. Int.,* **203,** 1738–1751.

Aubert, J., Aurnou, J. & Wicht, J., 2008. The magnetic structure of convection-driven numerical dynamos, *Geophys. J. Int.,* **172,** 945–956.

Aubert, J., Finlay, C.C. & Fournier, A., 2013. Bottom-up control of geomagnetic secular variation by the Earth's inner core, *Nature,* **502,** 219–223.

Backus, G., Parker, R. & Constable, C., 1996. *Foundations of Geomagnetism,* Cambridge Univ. Press.

Brendel, K., Kuipers, J., Barkema, G. & Hoyng, P., 2007. An analysis of the fluctuations of the geomagnetic dipole, *Phys. Earth planet. Int.,* **162**(3), 249–255.

Brown, W.J., 2015. Observations and characterisation of rapid variations in the Earth's internal magnetic field, *PhD thesis,* University of Leeds.

Buffett, B., 2015. Dipole fluctuations and the duration of geomagnetic polarity transitions, *Geophys. Res. Lett.,* **42,** 7444–7451.

Buffett, B. & Matsui, H., 2015. A power spectrum for the geomagnetic dipole moment, *Earth planet. Sci. Lett.,* **411,** 20–26.

Buffett, B.A., Ziegler, L. & Constable, C.G., 2013. A stochastic model for palaeomagnetic field variations, *Geophys. J. Int.,* **195,** 86–97.

Buffett, B.A., King, E.M. & Matsui, H., 2014. A physical interpretation of stochastic models for fluctuations in the Earth's dipole field, *Geophys. J. Int.,* **198,** 597–608.

Cheng, J. & Aurnou, J., 2016. Tests of diffusion-free scaling behaviors in numerical dynamo datasets, *Earth planet. Sci. Lett.,* **436,** 121–129.

Christensen, U.R. & Aubert, J., 2006. Scaling properties of convection-driven dynamos in rotating spherical shells and application to planetary magnetic fields, *Geophys. J. Int.,* **166,** 97–114.

Christensen, U.R. & Tilgner, A., 2004. Power requirements of the geodynamo from ohmic losses in numerical and laboratory dynamos, *Nature,* **429,** 169–171.

Christensen, U.R., Wardinski, I. & Lesur, V., 2012. Timescales of geomagnetic secular acceleration in satellite field models and geodynamo models, *Geophys. J. Int.,* **190,** 243–254.

Constable, C. & Johnson, C., 2005. A paleomagnetic power spectrum, *Phys. Earth Planet. Int.,* **153,** 61–73.

Constable, C. & Parker, R., 1988a. Smoothing, splines and smoothing splines; their application in geomagnetism, *J. Comput. Phys.,* **78**(2), 493–508.

Constable, C.G. & Parker, R.L., 1988b. Statistics of the geomagnetic secular variation for the past 5 m.y., *J. geophys. Res.,* **93**(B10), 11 569–11 581.

Davies, C.J. & Constable, C.G., 2014. Insights from geodynamo simulations into long-term geomagnetic field behaviour, *Earth planet. Sci. Lett.,* **404,** 238–249.

De Santis, A., Barraclough, D. & Tozzi, R., 2003. Spatial and temporal spectra of the geomagnetic field and their scaling properties, *Phys. Earth planet. Int.,* **135,** 125–134.

Dormy, E., 2016. Strong-field spherical dynamos, *J. Fluid Mech.,* **789,** 500–513.

Finlay, C.C. & Jackson, A., 2003. Equatorially dominated magnetic field change at the surface of Earth's core, *Science,* **300**(5628), 2084–2086.

Finlay, C.C., Olsen, N., Gillet, N. & Jault, D., 2013. Rapid core field variations during the satellite era: investigations using stochastic processes based field models, AGU Fall meeting, abstract #GP53C-1150.

Fournier, A., Nerger, L. & Aubert, J., 2013. An ensemble Kalman filter for the time-dependent analysis of the geomagnetic field, *Geochem. Geophys. Geosyst.,* **14**(10), 4035–4043.

Fournier, A., Aubert, J. & Thébault, E., 2015. A candidate secular variation model for IGRF-12 based on Swarm data and inverse geodynamo modelling, *Earth Planets Space,* **67**(1), 81, doi:10.1186/s40623-015-0245-8.

Frisch, U., 1995. *Turbulence: The Legacy of AN Kolmogorov,* Cambridge Univ. Press.

Gardiner, C.W., 1985. *Handbook of Stochastic Methods for Physics, Chemistry and the Natural Sciences,* Springer.

Gillet, N., Jault, D., Canet, E. & Fournier, A., 2010. Fast torsional waves and strong magnetic field within the Earth's core, *Nature,* **465,** 74–77.

Gillet, N., Jault, D., Finlay, C.C. & Olsen, N., 2013. Stochastic modelling of the Earth's magnetic field: inversion for covariances over the observatory era, *Geochem. Geophys. Geosyst.,* **14,** 766–786.

Gillet, N., Barrois, O. & Finlay, C., 2015. Stochastic forecasting of the geomagnetic field from the COV-OBS.x1 geomagnetic field model, and candidate models for IGRF-12, *Earth Planets Space,* **67**(1), 71, doi:10.1186/s40623-015-0225-z.

Greenspan, H.P., 1968. *The Theory of Rotating Fluids,* CUP Archive.

Hellio, G., 2015. Stochastic modeling of archeomagnetic measurements, *PhD thesis,* Université Grenoble Alpes.

Hellio, G., Gillet, N., Bouligand, C. & Jault, D., 2014. Stochastic modelling of regional archaeomagnetic series, *Geophys. J. Int.,* **199**(2), 931–943.

Holme, R. & Olsen, N., 2006. Core surface flow modelling from high-resolution secular variation, *Geophys. J. Int.,* **166**(2), 518–528.

Holme, R., Olsen, N. & Bairstow, F., 2011. Mapping geomagnetic secular variation at the core–mantle boundary, *Geophys. J. Int.,* **186**(2), 521–528.

Hulot, G. & Bouligand, C., 2005. Statistical palaeomagnetic field modelling and symmetry considerations, *Geophys. J. Int.,* **161**(3), 591–602.

Hulot, G. & Le Mouël, J., 1994. A statistical approach to the Earth's main magnetic field, *Phys. Earth planet. Int.,* **82**(3), 167–183.

Jackson, A., Jonkers, A.R.T. & Walker, M.R., 2000. Four centuries of geomagnetic secular variation from historical records, *Phil. Trans. R. Soc. Lond., A,* **358,** 957–990.

Jazwinski, A.H., 2007. *Stochastic Processes and Filtering Theory,* Dover Publications.

Kageyama, A., Miyagoshi, T. & Sato, T., 2008. Formation of current coils in geodynamo simulations, *Nature,* **454**(7208), 1106–1109.

King, E.M. & Buffett, B.A., 2013. Flow speeds and length scales in geodynamo models: the role of viscosity, *Earth planet. Sci. Lett.,* **371,** 156–162.

Korte, M. & Constable, C., 2011. Improving geomagnetic field reconstructions for 0–3 ka, *Phys. Earth planet. Int.,* **188,** 247–259.

Korte, M., Donadini, F. & Constable, C., 2009. Geomagnetic field for 0–3 ka: 2. A new series of time-varying global models, *Geophys. Geochem. Geosyst.,* **10**(6), doi:10.1029/2008GC002297.

Kuipers, J., Hoyng, P., Wicht, J. & Barkema, G., 2009. Analysis of the variability of the axial dipole moment of a numerical geodynamo model, *Phys. Earth planet. Int.,* **173,** 228–232.

Lesur, V., Wardinski, I., Rother, M. & Mandea, M., 2008. GRIMM: the GFZ Reference Internal Magnetic Model based on vector satellite and observatory data, *Geophys. J. Int.,* **173,** 382–394.

Lhuillier, F., Aubert, J. & Hulot, G., 2011a. Earth's dynamo limit of predictability controlled by magnetic dissipation, *Geophys. J. Int.,* **186,** 492–508.

Lhuillier, F., Fournier, A., Hulot, G. & Aubert, J., 2011b. The geomagnetic secular-variation timescale in observations and numerical dynamo models, *Geophys. Res. Lett.,* **38,** L09306, doi:10.1029/2011GL047356.

Lowes, F., 1974. Spatial power spectrum of the main geomagnetic field, and extrapolation to the core, *Geophys. J. R. astr. Soc.,* **36,** 717–730.

MacKay, D. J. C., 1998. Introduction to Gaussian processes, in *Neural Networks and Machine Learning,* vol. 168, pp. 133–165, ed. Bishop, C.M., Springer.

Mandea, M., Holme, R., Pais, A., Pinheiro, K., Jackson, A. & Verbanac, G., 2010. Geomagnetic jerks: rapid core field variations and core dynamics, *Space Sci. Rev.,* **155,** 147–155.

Meduri, D.G. & Wicht, J., 2016. A simple stochastic model for dipole moment fluctuations in numerical dynamo simulations, *Front. Earth Sci.,* **4,** doi:10.3389/feart.2016.00038.

Olson, P., Christensen, U. & Driscoll, P., 2012. From superchrons to secular variation: a broadband dynamo frequency spectrum for the geomagnetic dipole, *Earth planet. Sci. Lett.,* **319–320,** 75–82.

Panovska, S., Finlay, C. & Hirt, A., 2013. Observed periodicities and the spectrum of field variations in Holocene magnetic records, *Earth planet. Sci. Lett.,* **379,** 88–94.

Percival, D.B. & Walden, A.T., 1993. *Spectral Analysis for Physical Applications: Multitaper and Conventional Univariate Techniques,* Cambridge Univ. Press.

Riedel, K.S. & Sidorenko, A., 1995. Minimum bias multiple taper spectral estimation, *IEEE Trans. Signal Process.,* **43**(1), 188–195.

Roberts, P., Jones, C. & Calderwood, A., 2003. Energy fluxes and ohmic dissipation in the earth's core, in *Earth's Core and Lower Mantle,* pp. 100–129, eds Jones, C., Soward, A. & Zhang, K., Taylor & Francis.

Schaeffer, N., 2013. Efficient spherical harmonic transforms aimed at pseudospectral numerical simulations, *Geochem. Geophys. Geosyst.,* **14**(3), 751–758.

Schaeffer, N., 2015. *Exploring the Physics of the Earth's Core with Numerical Simulations,* Habilitation à diriger des recherches, Université Grenoble Alpes.

Soderlund, K.M., King, E.M. & Aurnou, J.M., 2012. The influence of magnetic fields in planetary dynamo models, *Earth planet. Sci. Lett.,* **333,** 9–20.

Takahashi, F. & Shimizu, H., 2012. A detailed analysis of a dynamo mechanism in a rapidly rotating spherical shell, *J. Fluid Mech.,* **701,** 228–250.

Tanriverdi, V. & Tilgner, A., 2011. Global fluctuations in magnetohydrodynamic dynamos, *New J. Phys.,* **13**(3), 033019, doi:10.1088/1367-2630/13/3/033019.

Thébault, E. & Gallet, Y., 2010. A bootstrap algorithm for deriving the archeomagnetic field intensity variation curve in the Middle East over the past 4 millennia BC, *Geophys. Res. Lett.,* **37,** L22303, doi:10.1029/2010GL044788.

Thomson, D.J., 1982. Spectrum estimation and harmonic analysis, *Proc. IEEE,* **70**(9), 1055–1096.

Van Kampen, N.G., 2007. *Stochastic Processes in Physics and Chemistry,* Elsevier.

Welch, P., 1967. The use of fast Fourier transform for the estimation of power spectra: a method based on time averaging over short, modified periodograms, *IEEE Trans. Audio Electroacoust.,* **15,** 70–73.

Yaglom, A.M., 2004. *An Introduction to the Theory of Stationary Random Functions,* Dover Publications.

Ziegler, L., Constable, C., Johnson, C. & Tauxe, L., 2011. PADM2M: a penalized maximum likelihood model of the 0–2 Ma palaeomagnetic axial dipole moment, *Geophys. J. Int.,* **184**(3), 1069–1089.

APPENDIX A: MAXIMUM LIKELIHOOD ESTIMATION OF LAW PARAMETERS FOR τ_n AND R_n

Within the maximum likelihood approach developed by Lhuillier *et al.* (2011b), the Gauss coefficients are assumed to be the result of a random Gaussian stationary process with a zero mean and a variance that depends only on the degree *n*. Given these assumptions, Lhuillier *et al.* (2011b) showed that the quantity $(\tau_n/\bar{\tau}_n)^2$ follows an F-distribution (also known as a Fisher–Snedecor distribution) with $((2n + 1)N_n, (2n + 1)N_n)$ degrees of freedom, noted $F^{(2n+1)N_n,(2n+1)N_n}$, with $\bar{\tau}_n$ the expectation of the timescale τ_n and N_n the number of independent values in the Gauss coefficient timeseries. N_n is equal to 1 when τ_n is estimated from an instantaneous model or a model covering a time-period shorter than $3\tau_n$. N_n equals $T/(3\bar{\tau}_n)$ for time-series of duration T longer than $3\tau_n$. Following Lhuillier *et al.* (2011b), the probability of a law (δ, γ) given the observed timescale τ_n^{obs} for degrees N_0 to N is

$$f(\delta, \gamma) = \prod_{n=N_0}^{N} F^{(2n+1)N_n,(2n+1)N_n} \left[\left(\frac{\tau_n^{\mathrm{obs}}}{\delta n^{-\gamma}} \right)^2 \right]. \tag{A1}$$

Because the likeliest value of the probability density function $f^{K,K}$ is $(K - 2)/(K + 2)$ for $K > 2$, the maximum likelihood estimate of (δ, γ) are the parameters that provide the maximum value of

$$f(\delta, \gamma) = \prod_{n=N_0}^{N} F^{(2n+1)N_n,(2n+1)N_n} \left[\frac{(2n + 1)N_n - 2}{(2n + 1)N_n + 2} \left(\frac{\tau_n^{\mathrm{obs}}}{\delta n^{-\gamma}} \right)^2 \right]. \tag{A2}$$

The parameters (α, β) of eq. (16) can be estimated using a similar approach. Within the assumptions of Lhuillier *et al.* (2011b), the quantity $(2n + 1)R/\bar{R}_n$ follows a χ^2-distribution with $(2n + 1)N_n$ degrees of freedom, noted $G^{(2n+1)N_n}$. The likeliest value of the χ^2 probability density function G^K is $K - 2$ for $K > 2$. Therefore, the maximum likelihood estimate of (α, β) are the parameters that provide the maximum value of

$$f(\alpha, \beta) = \prod_{n=N_0}^{N} G^{(2n+1)N_n} \left[((2n + 1)N_n - 2) \frac{R^{\mathrm{obs}}}{\alpha\beta^n} \right]. \tag{A3}$$

The probability density functions defined in eqs (A3) and (A2) and shown in Figs A1 and A2 for simulation S0 display a single maximum showing that this method provides a unique result. Note however that the parameter spaces delimited by the contour lines of the probability density functions deduced from the different estimates may not overlap. This is the case for the two averaged estimates of τ_n (Fig. A1) suggesting that the assumption of zero mean for the Gauss coefficients is not correct. The contour lines are elongated in an oblique direction showing that errors on parameters are correlated (errors on one parameter can be compensated by errors on the other parameters). As expected, the parameter space delimited by the contour lines is larger when using the instantaneous estimates of $\hat{R}_n$ and $\hat{\tau}_n$, which emphasizes that the estimated law is in this case less accurate.
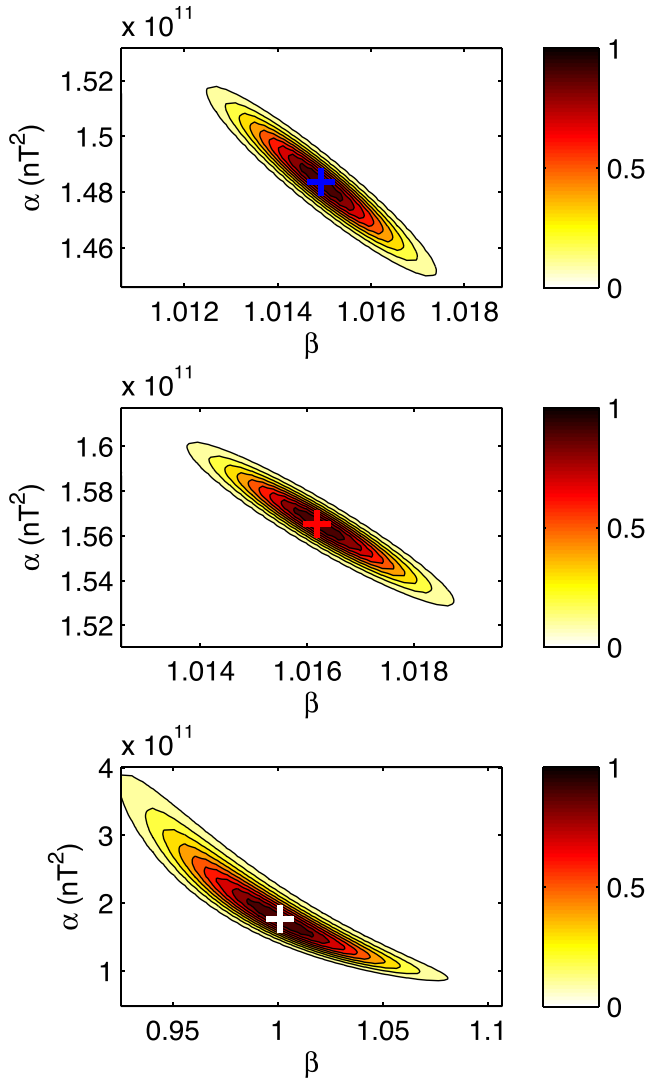
Figure A1. Probability density functions (normalized by their maximum value) for values of α and β (see eq. 16) for the S0 simulation deduced from R_n^* estimated using Gauss coefficients after subtracting their averaged value (top), from $\bar{R}_n$ using original Gauss coefficients (middle), and from an instantaneous $\hat{R}_n$ (bottom). Crosses indicate the maximum likelihood parameters.

Figure A2. Probability density functions (normalized by their maximum value) for values of δ and γ (see eq. 16) for the S0 simulation deduced from averaged τ_n^* estimated using Gauss coefficients after subtracting their averaged value (top), from $\bar{\tau}_n$ using original Gauss coefficients (middle), and from an instantaneous $\hat{\tau}_n$ (bottom). Crosses indicate the maximum likelihood parameters.

APPENDIX B: RELAXING THE HYPOTHESES $\beta = 1$ AND $\gamma = 1$

Fits of R_n and τ_n in Section 3.2 have been obtained assuming the restricting hypothesis $\beta = \gamma = 1$ in eq. (16). Here, we discuss how those regressions are modified once relaxing these constraints. This test is motivated by the derivation, from current geomagnetic field models, of larger (resp. lower) values for γ (resp. β). In particular, regression of τ_n from recent geomagnetic field models for degrees $n \geq 3$ gives $\gamma \simeq 1.45$ (Holme & Olsen 2006). A slightly lower value is obtained when including degree 2 in the regression.

For all estimates of R_n and τ_n and each simulation, we searched for the parameters (α, β) and (δ, γ) from eq. (16) for $n \in [2, 13]$. We used both the least-squares and the maximum likelihood methods. Results of the parameter search are summarized in Tables B1 and B2 and Fig. B1. As already observed by Lhuillier *et al.* (2011b), the results from the least-squares inversion and the maximum likelihood approach do not differ much.

The three simulations, run for different dimensionless parameters, provide different values of (α, β) and (δ, γ). Both S0 and CE show almost flat CMB spectra ($\beta \simeq 1$), whereas R_n is slightly decreasing with n ($\beta \simeq 0.9$) for S1. The values of γ for our simulations range from 0.75 to 1.3 (from average spectra), encompassing the value $\gamma = 1$ favoured by Lhuillier *et al.* (2011b) and found for the CE simulation. The most extreme (lowest viscosity, strongest forcing) simulation S1 shows the steepest decrease of τ_n with n (larger value of γ). S1 thus gives the closest value of γ to the instantaneous estimate from geomagnetic observations. For CE and S1, γ is decreased by about 5 per cent when removing the time-average Gauss coefficients in the estimations of R_n and τ_n. Despite its relatively modest forcing and viscosity and its specific torque and heat flux conditions, the simulation CE nevertheless presents a correlation time τ_n more sensitive to n than S0. Estimated values for δ encompass $\tau_{SV} = 415$ yr (τ_{SV} is defined as δ for $\gamma = 1$). This time differs from τ_{SV} in the simulations S0 and S1, for which γ

Table B1. Parameters (α, β) for simulations S0, CE and S1, estimated from the least-squares (LSQ) and maximum likelihood (ML) approaches. α is expressed in 10^9 nT^2 and β is dimensionless. (a) Estimated from snapshot values $\hat{R}_n$ (average value $\pm$ standard deviation, for 10 independent epochs); and from the expected variances as in eq. (15), either removing (c) or keeping (b) the average value of the coefficients.

| | | α | | β | |
		LSQ	ML	LSQ	ML
	(a)	147.0 ± 107.5	156.1 ± 86.3	1.05 ± 0.07	1.03 ± 0.05
S0	(b)	152.6	156.5	1.02	1.02
	(c)	143.1	148.4	1.02	1.01
	(a)	10.2 ± 5.9	11.0 ± 5.3	1.00 ± 0.05	0.99 ± 0.04
CE	(b)	10.3	11.2	0.99	0.99
	(c)	8.6	9.7	1.01	1.00
	(a)	33.2 ± 16.6	42.5 ± 20.1	0.93 ± 0.04	0.91 ± 0.03
S1	(b)	37.5	37.7	0.91	0.91
	(c)	27.7	27.3	0.93	0.93

Table B2. Parameters (δ, γ) for simulations S0, CE and S1, estimated from the least-squares (LSQ) and maximum likelihood (ML) approaches. δ is expressed in years (and in terms of τ_{SV} in parentheses) and γ is dimensionless. (a) Estimated from snapshot values $\hat{\tau}_n$ (average value $\pm$ standard deviation, for 10 independent epochs); and from the expected variances as in eq. (15), either removing (c) or keeping (b) the average value of the coefficients.

| | | δ | | γ | |
		LSQ	ML	LSQ	ML
	(a)	$313 \pm 154 (0.75 \pm 0.37)$	$278 \pm 128 (0.67 \pm 0.31)$	0.81 ± 0.18	0.75 ± 0.15
S0	(b)	294(0.71)	253(0.61)	0.86	0.78
	(c)	284(0.68)	248(0.60)	0.85	0.79
	(a)	$500 \pm 153 (1.20 \pm 0.37)$	$460 \pm 135 (1.11 \pm 0.33)$	1.07 ± 0.16	1.02 ± 0.16
CE	(b)	461(0.97)	415(1.00)	1.05	1.00
	(c)	401(0.97)	375(0.90)	0.99	0.96
	(a)	$835 \pm 426 (2.01 \pm 1.03)$	$939 \pm 409 (2.26 \pm 0.99)$	1.22 ± 0.27	1.29 ± 0.22
S1	(b)	704(1.70)	748(1.80)	1.23	1.26
	(c)	585(1.41)	592(1.43)	1.17	1.18
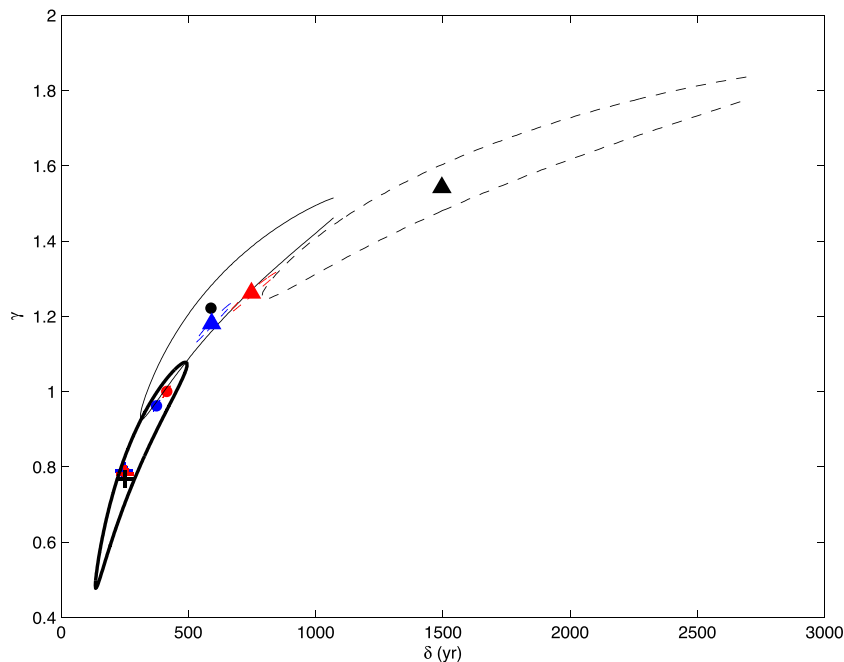
Figure B1. Curves of constant probability density (corresponding to 20 per cent of the maximum probability) and maximum probability in the plane (δ, γ) obtained with the maximum likelihood method for one snapshot of each simulation S0 (black thick line and cross), CE (black thin line and filled circle) and S1 (black dashed line and triangle). For comparison, we also show the maximum probabilities from time-averages obtained while keeping (red) or not (blue) the average. Note that the probability functions obtained from time-averages are also represented but are restricted to too small parameter space to be visible on this figure.

deviates significantly from 1, and it is close to τ_{SV} in the simulation CE for which $\gamma \simeq 1$.

If in average, parameters obtained from snapshot estimates $\hat{R}_n$ and $\hat{\tau}_n$ are mostly similar to those obtained using time-averaged, a r.m.s. mismatch of about 20 per cent (resp. 5 per cent) may be found between instantaneous and time-integrated estimates of the parameter γ (resp. β) defining the dependence of τ_n (resp. R_n) with the degree n. From Table B2, the two-sigma intervals found for γ in simulations S0, CE and S1 are respectively [0.45, 1.05], [0.70, 1.3] and [0.85, 1.7] using the maximum likelihood method of Appendix A. Similar ranges of values are obtained by computing the probability density function obtained from a single snapshot of τ_n, as illustrated in Fig. B1.